Quantum-dot-in-perovskite solids

Zhijun Ning, Xiwen Gong, Riccardo Comin, Grant Walters, Fengjia Fan, Oleksandr Voznyy, Emre Yassitepe, Andrei Buin, Sjoerd Hoogland & Edward H. Sargent

Quantum-dot-in-perovskite solids

Zhijun Ning[1†], Xiwen Gong[1], Riccardo Comin[1], Grant Walters, Fengjia Fan, Oleksandr Voznyy, Emre Yassitepe, Andrei Buin, Sjoerd Hoogland & Edward H. Sargent*

Department of Electrical and Computer Engineering, University of Toronto, 35 St. George Street. Toronto, Ontario, M5S 1A4, Canada

[1] These authors contribute equally to this work

E-mail: ted.sargent@utoronto.ca

† Current address: School of Pysical Science and Technology, ShanghaiTech University, Haike Road 100, 201210, Shanghai, China.

Heteroepitaxy is the basis of electrically-driven lasers, multijunction solar cells, and blue light-emitting diodes[1-5]. Crystalline coherence is preserved even when atomic identity is modulated, a fact that is the critical enabler of quantum wells, wires, and dots[6-10]. The interfacial quality achieved through heteroepitaxial growth allows new combinations of materials with complementary properties, enabling the design and realization of functionalities not available in the single-phase constituents. Here we show that organohalide perovskites and pre-formed colloidal quantum dots, combined in the solution phase, can produce epitaxially-aligned dots-in-a-matrix crystals. Using transmission electron microscopy and diffraction, we reveal heterocrystals as large as ~ 60 nm and containing at

least 20 mutually-aligned dots that inherit the crystalline orientation of the perovskite matrix. The heterocrystals exhibit remarkable optoelectronic properties traceable to their atom-scale crystalline coherence: photoelectrons and holes generated in the larger-bandgap perovskites are transferred with 80% efficiency to become excitons in the quantum dot nanocrystals, leveraging perovskites' excellent photocarrier diffusion to produce bright light emission from infrared-bandgap quantum-tuned materials. By combining the excellent electrical transport of the perovskite matrix and the high radiative efficiency of the quantum dots, we engineer a new platform to advance solution-processed infrared optoelectronics.

Atomically-aligned growth of a crystalline film atop a substrate – heteroepitaxy – has largely relied on vacuum methods such as molecular-beam epitaxy (MBE), atomic-layer epitaxy (ALE), and metalorganic vapour phase epitaxy (MOCVD)[1,2]. Through these methods, theoretical predictions have been tested and refined that describe conditions under which crystalline coherence can be preserved even in the presence of a mismatch in the native lattices (strained-layer epitaxy). The result is a vast body of theory, knowledge, and practice regarding vapour-phase epitaxy. Since interfacial defects can be rendered rare at suitably-designed hetero-interfaces, highly efficient luminescent materials have been created that have enabled efficient electrically-injected lasers and light-emitting diodes for fiber-optic communications and high-efficiency lighting[3-5].

The past two decades have seen the rapid rise of soft condensed matter, often in the form of solution-processed semiconductors based on organic molecules, polymers, and colloidal nanoparticles (plates, wires, and dots)[6-10]. In this vein, and with astonishing rapidity, bulk

organohalide semiconductor perovskites exhibiting large and perfect crystalline domains have improved in size, properties, and performance. These remarkable materials have enabled the ascent of the perovskite solar cell[11-13].

We posited that – under the right conditions – heteroepitaxial alignment could be produced between bulk perovskite semiconductors and quantum-tuned nanoparticles. Thin films comprising multi-material, yet internally-epitaxially-aligned, heterocrystals – complex crystals we herein term poly hetero crystalline (PHC) solids – could combine, without undue photocarrier loss, the desired properties of each phase: the excellent charge carrier transport of the bulk perovskites, and the quantum-tuned infrared luminescence of the quantum dot phase.

We sought to implement these ideas in a materials system that would show promise for epitaxial alignment, and would illustrate applied potential. From an applied perspective, methylammonium lead iodide perovskite ($MAPbI_3$) has led to the most efficient solution-processed solar cells reported. Colloidal quantum dots based on PbS have been widely shown to exhibit highly tunable photophysical properties, including in the near- and short-wavelength infrared which, today, the perovskites fail to access. From a materials science perspective, $MAPbI_3$ (tetragonal) and PbS (rocksalt) possess related crystal structures, each having a six-coordinated Pb atom, and with Pb-Pb distance (PbS 5.97 Å, $MAPbI_3$ 6.26 Å) that reside within 4.6% of one another[11].

Consequently, we hypothesized that, if formed from a combined, miscible solution phase into solid materials together (Fig. 1), the materials could potentially form PHC solids exhibiting optoelectronic properties that synergize the best features of each constituent material. Structurally, the PbS CQD lattice can match well with the perovskite structure both two-dimensionally (Fig. 1a)

and three-dimensionally (Fig. 1b). Pioneering studies have previously elucidated the synthesis and properties of composite organic/inorganic crystalline hybrids[14]; here we aim instead to engineer a heterocrystalline solid-state solution between two different, but structurally affine materials. Specifically, we were motivated herein by the opportunity to combine strong luminescent efficiency of the quantum dots with long-range carrier transport in the perovskite matrix.

To implement atomic-level coherence between the inorganic PbS and the organometallic $MAPbI_3$ phase, we would require an organic-ligand-free strategy for the capping of the PbS nanoparticles. With this in mind, we leveraged the recent synthesis of colloids stabilized not using traditional aliphatic ligands, but instead using halide ligands introduced from the perovskite precursor methylammonium iodide[15,16].

Structural affinity alone is necessary but not sufficient to offer epitaxial bonding between the two phases; energetic considerations must also be taken into account. Here we use density functional theory (DFT) to study the interface formation energy between PbS (100 facet) and perovskite (110 facet) (Extended Data Fig. 1)[17]. The interfacial energy is less than 10 meV/Å^2, suggesting that the growth of perovskite on PbS at room temperature is nearly as feasible as homoepitaxy of PbS-on-PbS or perovskite-on-perovskite. DFT further revealed that the epitaxial 3D embedding of PbS CQDs inside a perovskite matrix can be achieved without the formation of interfacial defects (Fig. 1c), i.e. the bandgap is predicted to remain open, with no in-gap defects predicted (Extended Data Fig. 2).

We therefore proceeded to design our strategy to build a PHC solid. We began by exchanging organic ligands on the PbS CQDs to short halide (iodide in this case) anionic ligands (Extended Data Fig. 6a). We then mixed these inorganically-terminated CQDs with PbI_2 dissolved

in butylamine, with this solvent strategy crucial to maintaining CQD surface passivation following film growth. Since PbI_2 forms a complex with iodide and binds to the CQD surface, PbI_2 and CQDs were, as expected, well able to mix in solution (transmittance spectra of the colloid showed no loss of optical transmission for photon energies below the CQD bandgap, indicating no increase in scattering and thus no appreciable solution-phase aggregate formation). By controlling the ratio of PbI_2 and CQDs, we tuned the nominal CQD concentration – hereafter expressed as the ratio of CQD to total volume – across the range 0.2% to 29% (see Extended Data Fig. 11a for a full list of values used in the present study). To fabricate the CQD:$MAPbI_3$ films (Extended Data Fig. 6b, 6c), we used the previously-established sequential (two-step) method[11], whereby the PbI_2:CQD films are initially deposited via spin-coating onto a glass substrate, and these are then soaked in a CH_3NH_3I/isopropanol solution. X-ray photoelectron spectroscopy (XPS) and Rutherford Backscattering Spectroscopy (RBS) were used to confirm the presence of both PbS and $MAPbI_3$ in the final film (Extended Data Fig. 4a-4d). We detected no trace of amine ligands associated with the solvent (Extended Data Fig. 4e). RBS (Extended Data Fig. 4f) was used to estimate the experimental CQD volume percentage as a function of nominal CQD:$MAPbI_3$ ratio.

High-resolution transmission electron microscopy (HRTEM) was used to characterize the crystal structure and orientation of both CQDs and perovskite matrix for a sample with nominal CQD volume percentage of 4%. Since $MAPbI_3$ is an organic/inorganic hybrid material with lower density than PbS, it shows much lower contrast than inorganic CQDs, thus facilitating differentiation among the perovskite and PbS phases. The higher contrast of CQDs was confirmed using high-angle annular dark field scanning transmission electron microscopy (HAADF-STEM), a direct probe of density variations in the material (see Extended Data Fig. 5 and corresponding discussion in the Methods). The contrast between CQDs and perovskite can be clearly observed in

the large field-of-view HRTEM map of Fig. 2a, while Fig. 2b shows the corresponding Fast Fourier transform (FFT), with lattice planes indexed as indicated in Fig. 2c. The contributions from the perovskite matrix vs. from the quantum dots can be distinguished by analyzing the subregions shown in Fig. 2d and 2g for the perovskite and quantum dots, respectively. Well-defined lattice fringes with 2.2 Å separation (Fig. 2d) can be indexed to the (224) plane of the matrix, as confirmed by the corresponding FFT images (Fig. 2e and 2f) which show that the real-space HRTEM image is projected along the $[2\bar{2}4]$ zone axis. We also measured the lattice fringes of the CQDs which show the same orientation and can be indexed as the (022) plane of PbS (2.1 Å), (Figs. 2g, 2h, 2i). This is consistent with simulations that show how the (100) facet of PbS matches well with (110) facet of perovskite. Strikingly, from FFT, the facet angles between (224) and [201] of the perovskite are the same as between the (022) and [111] facets of PbS. Hence, the orientation relationships between $MAPbI_3$ and CQDs can be identified as below:

$$(022)_{PbS} \parallel (224)_{MAPbI_3};\ [111]_{PbS} \parallel [201]_{MAPbI_3}.$$

From this we can conclude that the matrix and CQDs show the same orientation, readily observed both in real-space microscope images and confirmed using FFT. This analysis demonstrates epitaxial alignment between perovskite and CQDs. Even a slight misalignment would be revealed by the experimental maps, as suggested by TEM simulations of epitaxially-oriented vs. epitaxially-misoriented PHCs (Extended Data Fig. 6d, 6e)[18].

The optical absorption spectra for pure CQD films and for the new dot-in-perovskite PHCs are shown in Fig. 3a (absorption and emission spectra for pure CQD and pure perovskite films are also reported in Extended Data Fig. 7a, 7b). Absorption signatures corresponding to each constituent, perovskite and CQD, are readily apparent in the hybrid films (Fig. 3a). The

photoluminescence (PL) spectra show emission proper to CQDs in film (Fig. 3b), indicating that the photophysical properties of CQDs are kept intact when the CQDs are incorporated into the perovskite matrix. As CQD concentration increases, the absorption spectrum red-shifts, consistent with increased inter-dot interaction (potentially partial dot fusion at these high concentrations) which reduces the extent of quantum confinement and thus shrinks the bandgap. This affects absorption and luminescence to the same extent, i.e. it does not, to first order, impact the Stokes shift. A second effect is increased long-range excitonic and carrier transport from dot to dot, present only at the highest concentrations. Through this process, excitons and carriers are transferred to the smallest-gap dots in an inhomogeneously-broadened population. This effect does not impact absorption, but does red-shifts the luminescence, and thus increases Stokes shift[19,20]. An additional mechanism produces a blueshift (even relative to dots in solution) at low CQD loading: tensile strain caused by the lattice mismatch between CQDs and the perovskite slightly expands the PbS lattice, leading to an increase in bandgap[21]. This tensile strain acts to the same extent on absorption and emission. (See also Extended Data Fig. 3 and corresponding discussion in the Methods)

We then turned to investigating the CQD photoluminescence quantum efficiency (PLQE) – the ratio between emitted and absorbed photons – for a series of samples with different CQD concentrations. Initially we employed an excitation wavelength of 815 nm, i.e. below the absorption edge of the perovskite (Fig. 3d), to excite the quantum dot phase directly and exclusively. The PLQE is highest in low-dot-concentration samples, consistent with minimal quenching associated with the dissociation of excitons into free carriers in the neighboring quantum dots[22]. The PL quantum yield reaches 9.3%, which is fully two orders of magnitude higher than that in the pure CQD film. As a control to study the importance of lattice matching on

photophysical properties, we changed the matrix to sodium iodide (NaI) (rocksalt structure with 8.8% lattice mismatch with PbS): the PLQE of CQDs in a NaI matrix is almost two orders of magnitude lower than in perovskite matrix (Fig. 3d).

To elucidate the physical origins of enhanced PL efficiency for dots embedded in a perovskite matrix, we used DFT to investigate whether CQD surfaces can in principle be passivated using the perovskite matrix. Both the highest occupied molecular orbital (HOMO) and lowest unoccupied molecular orbital (LUMO) are located in the core of PbS CQDs, and the bandgap is trap-free. In contrast, for a CQD misaligned with the perovskite matrix, trap states are induced at the CQD surface, mostly on the conduction band side (Extended Data Fig. 2c, 2d, 2f).

In addition to providing passivation, the matrix:dot interface will be the critical enabler of any charge carrier injection into the CQDs. To study carrier transfer across this interface, we relied on ~4 nm diameter CQDs (bandgap of 1 eV) whose LUMO energy level is predicted to lie below the conduction band of the perovskite and whose HOMO should reside above the valence band edge of the perovskite (Fig. 4a).

By generating excitons in the dots only (via photoexcitation using photon energies lower than the perovskite bandgap), and in separate studies instead photogenerating principally in the perovskite matrix, we investigate carrier transfer to, and across, the CQD-perovskite interface. Photoluminescence excitation spectra (PLE, Fig. 4b) reveal enhanced CQD emission when the perovskite is excited ($\lambda_{excitation} \lesssim 780\ nm$)[23]. Increased perovskite content drives a higher CQD PL intensity when the excitation occurs in the perovskite absorption region. This qualitatively indicates efficient charge diffusion to, and across, the perovskite-CQD interface. Carrier transfer also occurs in other composite nanomaterials[22,24], such as in materials made up of small-bandgap-

CQD inclusions in a large-bandgap-CQD matrix; however, we found that the use of a perovskite matrix provided superior passivation of the quantum dot centers as evidenced by the nearly two orders of magnitude higher PLQE compared to an NaI matrix, and, commensurably, by the 5-fold increase in carrier lifetime compared to dots-in-dots films (for more details see Figure S20).

The signatures of carrier transfer from the matrix to the quantum dots are also evident in the PL emission from $MAPbI_3$ in PHC films as a function of CQDs concentration (Fig. 4c). In particular, for concentrations above 0.4%, we observe a complete quenching of the perovskite PL signal, consistent with a highly efficient removal of photogenerated carriers from the matrix and transfer into the dots. At higher CQD concentrations, i.e. in the regime of low densities of injected carriers per dot where radiative recombination is dominant over higher-order (e.g., Auger) processes, we can quantitatively estimate the carrier transfer efficiency from perovskite to CQDs based on PL and absorption data (Extended Data Fig. 11b and discussion in Methods). The transfer efficiency attains a remarkable value exceeding 80% at the highest CQD loading (28% CQD volume percentage).

We investigated the carrier dynamics in the PHC using PL decay (Fig. 4d, 4e). We used a two-component decay model to analyze transient PL. The fast decay transient in CQDs is assigned to fast exciton dissociation into neighboring CQDs, while the longer dynamics are ascribed to radiative recombination. The comparison between the PHC and the pure CQD PL transients in Fig. 4e shows a dramatic slowdown of exciton dissociation dynamics as soon as the CQDs are embedded in the perovskite matrix (from sub-ns in pure CQD to 20 ns in PHC at high CQD loading). Furthermore, the fast transient component increases from 20 ns to 70 ns as the CQD concentration is reduced (see Fig. 4f) and correspondingly the inter-dot separation is increased, consistent with the expected suppression in the exciton dissociation rate for more isolated dots.

The perovskite carrier dynamics (Fig. 4d) show a rapid quenching of the PL emission, from 25 ns in pure $MAPbI_3$ to ~2 ns in the PHC film at lowest CQD loading. The PL lifetime associated with emission from the perovskite phase in quantum-dot-in-perovskite solids is highest (2 ns) at the lowest CQD concentration studied herein (Fig. 4f). At this lowest concentration, the inter-quantum-dot spacing is an estimated 40 nm, and this relatively larger separation increases the time for photocarriers to diffuse from their point of photogeneration in the perovskite phase to the point of capture into a quantum dot (see also Extended Data Fig. 10). We use the term "charge carrier" when referring to photoexcitations in the perovskite phase since prior studies have revealed that photogenerated excitons in perovskite separate to become free carriers within about 2 picoseconds following generation[25]. This analysis does not, of course, preclude the possibility that, especially for those excitons generated very near to a quantum dot, some fraction of excitations could transfer as excitons from perovskite to dot.

This work reports an *in-situ* epitaxial growth process of perovskite on quantum dot surfaces. The quantum dots are effectively passivated by the matrix, without the need for conventional organic ligands, when lattice-matching conditions are fulfilled. At the same time, the perovskite matrix provides excellent carrier transport to the CQDs thanks to its superior diffusion length. The new approach paves the way for novel strategies to enhance the performance of CQD-based optoelectronic devices, and to extend towards the infrared the spectral diversity of perovskite-based materials.

Acknowledgements

This publication is based in part on work supported by an award (KUS-11-009-21) from the King Abdullah University of Science and Technology (KAUST), by the Ontario Research Fund

Research Excellence Program and by the Natural Sciences and Engineering Research Council (NSERC) of Canada. Computations were performed using the BlueGene/Q supercomputer at the SciNet HPC Consortium provided through the Southern Ontario Smart Computing Innovation Platform (SOSCIP). E.Y. acknowledges support from FAPESP-BEPE (14/18327-9) fellowship. The authors thank Levina L. for the assistance in CQDs synthesis, Beauregard E. for the assistance in PHC synthesis, Z. Yang, M. Adachi, for helpful discussion. Palmiano E., Wolowiec R., and Kopilovic D. for their help during the course of study.

References:

1. Pohl, U. W. *Epitaxy of Semiconductors* (Springer, 2013).

2. McCray, W. P. MBE deserves a place in the history books. *Nature Nanotech.* **2,** 259-261 (2007).

3. Huang, M. H. *et al.* Room-temperature ultraviolet nanowire nanolasers. *Science* **292,** 1897 (2001).

4. Choi, K., Kako, S., Holmes, M. J., Arita, M. & Arakawa, Y. Strong exciton confinement in site-controlled GaN quantum dots embedded in nanowires. *Appl. Phys. Lett.* **103,** 171907 (2013).

5. Adhikari, H., Marshall, A. F., Chidsey, C. E. D. & Mcletyre, P.C. Germanium nanowire epitaxy: shape and orientation control. *Nano Lett.* **6,** 318-323 (2006).

6. Diao, Y. *et al.* Solution coating of large-area organic semiconductor thin films with aligned single-crystalline domains. *Nature Mater.* **12,** 665-671 (2013).

7. Shirasaki, Y., Supran, G. J., Bawendi, M. G. & Bulović, V. Emergence of colloidal quantum-dot light-emitting technologies. *Nature Photon.* **7,** 13-23 (2013).

8. Grätzel, M., Janssen, R. A. J., Mitzi, D. B. & Sargent, E. H. Materials interface engineering for solution-processed photovoltaics. *Nature* **488,** 304-312 (2012).

9. Talapin, D. V., Lee, J., Kovalenko, M. V. & Shevchenko, E. V. Prospects of colloidal nanocrystals for electronic and optoelectronic applications. *Chem. Rev.* **110,** 389-458 (2010).

10. Ma, W., Luther, J., Zheng, H., Wu, Y. & Alivisatos,P. *Nano Lett.* **9,** 1699-1703 (2009).

11. Burschka, J. *et al.* Sequential deposition as a route to high-performance perovskite-sensitized solar cells. *Nature* **499,** 316-319 (2013)

12. Tan, Z. *et al.* Bright light-emitting diodes based on organometal halide perovskite. *Nature Nanotech.* **9,** 687-692 (2014).

13. Stranks, S. D. *et al.* Electron-hole diffusion lengths exceeding 1 micrometer in an organometal trihalide perovskite absorber.*Science* **342,** 341-344 (2013).

14. Mitzi, D. B. Chondroudis, K. and Kagan, C. R. Organic-inorganic electronics, *IBM J. Res. Dev*. **45**, 29 (2001).

15. Ning, Z., Dong, H., Zhang, Q., Voznyy, O. & E. H. Sargent. Solar cells based on inks of n-type colloidal quantum dots. *ACS Nano* **8,** 10321-10327 (2014).

16. Dirin, D. N. *et al.* Lead halide perovskites and other metal halide complexes as inorganic capping ligands for colloidal nanocrystals. *J. Am. Chem. Soc.* **136,** 6550-6553 (2014).

17. Leitsmann, R., Böhm, O., Plänitz, P., Radehaus, C., Schaller, M. & Schreiber, M. Adsorption mechanisms of fluorocarbon polymers at ultra low-k surfaces. *Surf. Sci.* **604,** 1808-1812 (2010).

18. C. Koch. Determination of core structure periodicity and point defect density along dislocations. Arizona State University. (2002).

19. Moroz, P. *et al.* Suppressed carrier scattering in CdS-encapsulated PbS nanocrystal films. *ACS Nano* **7,** 6964–6977 (2013).

20. Gao, Y. *et al.* Enhanced hot-carrier cooling and ultrafast spectral diffusion in strongly coupled PbSe quantum-dot solids. *Nano Lett.* **11,** 5471–5476 (2011).

21. Wise, F. W. Lead salt quantum dots: the limit of strong quantum confinement. *Acc. Chem. Res.***33,** 773-780 (2000).

22. J. J. Choi, J. Luria, B.-R. Hyun, A. C. Bartnik, L. Sun, Y.-F. Lim, J. A. Marohn, F. W. Wise & T. Hanrath, Photogenerated Exciton Dissociation in Highly Coupled Lead Salt Nanocrystal Assemblies. *Nano Lett.* **10,** 1805–1811 (2010).

23. Kagan, C. R., Murray, C. B., Nirmal, M., & Bawendi, M. Electronic energy transfer in CdSe quantum dot solids, *Phys. Rev. Lett.* **76**, 1517-1520 (1996).

24. F. Xu, X. Ma, C. R. Haughn, J. Benavides, M. F. Doty & S. G. Cloutier, Efficient Exciton Funneling in Cascaded PbS Quantum Dot Superstructures. *ACS Nano* **5,** 9950–9957 (2011).

25. Ponseca, C. S. *et al.* Organometal halide perovskite solar cell materials rationalized: ultrafast charge generation, high and microsecond-long balanced mobilities, and slow recombination. *J. Am. Chem. Soc.* **136,** 5189–92 (2014).

Author contributions

Z.N., X.G., R.C., and E.H.S. designed and directed this study. Z.N. and X.G. contributed to all the experimental work. R.C. carried out the PL lifetime and PL excitation measurements and analysis. G. W. and S. H. performed PLQE and the carrier transfer efficiency study. F. F. and E.Y. did the TEM measurement and FFT analysis. O.V. carried out the TEM simulation, XPS measurement.

O.V. and A.B. performed DFT simulation. Z.N., X.G., R.C. and E.H.S. wrote the manuscript. All authors commented on the paper**.**

Additional Information

Reprints and permissions information is available online at www.nature.com/reprints. Correspondence and requests for materials should be addressed to E.H.S.

Competing financial interests

The authors declare no competing financial interests.

Methods

CQD synthesis and solution ligands exchange

Colloidal quantum dots (CQDs) were synthesized using methods previously reported[1]. For iodide ligand exchange, 3 mL of CQDs dispersed in octane (10 mg/mL) were added into 3 mL of dimethylformamide (DMF) solution containing 350 mg of PbI_2 and 150 mg of CH_3NH_3I. After stirring for 10 minutes, CQDs had transferred from the top octane phase to the bottom DMF. After removing the octane, we washed the CQD solution three more times using octane to remove the organic residue. Subsequently the CQDs were precipitated by the addition of toluene. The nanoparticles were dispersed in butylamine for film fabrication.

Poly heterocrystalline (PHC) solids fabrication

A given amount of PbI_2 (with one quarter weight ratio of CH_3NH_3I) was added into the solution for perovskite growth. A spin coating process was used for film fabrication (spin speed of 6000 rpm). The film was then annealed at 70 degrees for 10 minutes in N_2 glovebox. For perovskite

growth, methylammonium iodide solution (10 mg/mL in isopropanol) was dropped and left on the film for 30 seconds. After removing the solution by spin coating (spin speed 6000 rpm), the film was soaked in pure isopropanol for 10 sec, and then a spin coating process was performed to remove the residual solvent. In the end, the film was annealed again at 70 degrees for 10 minutes in N_2 glovebox.

Density Functional Theory (DFT) simulations

Calculations were performed within the Density Functional Theory (DFT) formalism using the Perdew-Burke-Ernzerhof (PBE)[2] GGA exchange correlation functional. All calculations were performed utilizing the CP2K[3] package with mixed Gaussians and plane waves basis set, using the molecularly optimized MOLOPT[3] double ζ-valence polarized (mDZVP) basis set implemented in CP2K code which has very small basis set superposition errors (BSSE) in gas and condensed phases[4-7]. The charge density cut-off was 300 Ry, which is suitable for the Goedecker-Teter-Hutter pseudopotentials.[8] Spin polarized (LSDA) and spin-unpolarized calculations (LDA) were performed in the case of the odd and even number of electrons, respectively. The structural minimization was performed with the help of the Broyden-Fletcher-Goldfarb-Shanno algorithm[9] (BFGS). Surface slabs were modelled as (110) $MAPbI_3$of tetragonal structure and (100) cubic PbS with 7 monolayers each.100 Å of vacuum were added on top of the slab. Dipole correction was used to remove artificial dipole-dipole interaction across periodic images as implemented in the CP2K v2.5. A 3x3 (26.88 Å x 26.88 Å) supercell was used in the xy-plane.

The interfacial energy was computed using the relation[10]:

$$E_{inter}^{MAPbI_3/PbS} = E_s(MAPbI_3) + E_s(PbS) - E_{Ad.}(MAPbI_3/PbS) \quad (1)$$

where E_s represents the surface energies of the corresponding surfaces ($MAPbI_3$ and PbS, respectively), and E_{Ad} ($MAPbI_3$/PbS) is the adsorption energy of the $MAPbI_3$ on PbS. It describes the energy required to cut the PbS and $MAPbI_3$ bulk and combine the obtained free surfaces to form the MAPbI3/PbS interface.

The estimated surface energy of the PbS(100) is 9 meV/Å^2 which is in close agreement with previously reported[11] values of 12 meV/Å^2. The $MAPbI_3$ surface energy is[12,13] 9 meV/Å^2. The adsorption energy is calculated via:

$$E_{Ad.}^{MAPbI_3/PbS} = E_{slab}(MAPbI_3) + E_{slab}(PbS) - E_{slab}(MAPbI_3/PbS) \quad (2)$$

where E_{slab} are the slab energies of the corresponding bare $MAPbI_3$ and PbS slabs, whereas E_{slab}($MAPbI_3$/PbS) is the energy of the combined PbS/$MAPbI_3$ slab. The adsorption energy is calculated to be around the 12 meV/Å^2, which gives value of the interfacial energy on the order of the 6 meV/Å^2. The value obtained for the interfacial energy, which is smaller than that of free surfaces, is indicative of the matched interface being favored over broken bonds at the interface.

Calculations investigating the case of a PbS CQD embedded in a perovskite matrix were performed using a 50.6 Å^3 box that contained ~3000 atoms. The relaxed lattice constant of the perovskite was imposed on the unit cell, corresponding to ~5% tensile strain on PbS. A PbS CQD of ~3 nm diameter fully relaxed in vacuum was placed inside a manually prepared cavity in perovskite providing an epitaxial matching. Fully quantum mechanical total energy minimization was performed on the combined system.

We find that the PbS lattice constant is changed by only 0.5% strain instead of by the imposed 5% difference between its lattice constant and that of the perovskite (see Extended Data Fig. 3). Instead the preponderance of lattice constant change is accommodated in the perovskite in a thin layer

within 1 or 2 lattice constant near the interface. This can be explained by the fact that PbS is much stiffer than perovskite: bulk modulu s B_{PbS}= 127 GpA[14] while $B_{perovskite}$=12.2 GPa[15]. Calculated bandgaps for strained PbS 3 nm CQD in vacuum are: E_g[no strain] = 1.06 eV, and E_g[0.5% tensile strain] = 1.08 eV, consistent with deformation potentials derived from temperature dependent bandgaps for these QD sizes[16].

This corresponds to ~24 nm blueshift, consistent with the excess blueshift observed experimentally in low-loading samples over and above the shift associated with low dot-to-dot communication.

Decoupling of perovskite and CQD contribution in electron microscopy

We utilized high-angle annular dark field scanning transmission electron microscopy (HAADF-STEM) to image the dots in perovskite. The corresponding signal, which originates from electrons that are scattered incoherently at large angles, provides contrast between the heavier (denser) CQDs and the lighter $MAPbI_3$ matrix. Under these conditions, contributions from diffraction and phase are suppressed, and the contrast therefore depends mainly on the atomic number Z. Consequently, the denser PbS QDs will scatter electrons more strongly, yielding a higher intensity at the detector than when imaging the perovskite crystal matrix. This contrast can be seen in the HAADF-STEM map of a CQD:perovskite thin film with 3.9% CQD loading (Extended Data Fig. 5c), with brighter regions marking the presence of QDs having ~5 nm diameter. The absence of these intensity variations in a pure perovskite matrix is shown in Extended Data Fig. 5a, which images a single perovskite grain (white region) in which no brightness fluctuations are observed. The corresponding HRTEM maps are shown in Extended Data Fig. 5b (pure perovskite film) and in the inset of Extended Data Fig. 5c (CQD:perovskite thin film). In the latter, the HRTEM is only acquired in the region highlighted by the yellow circle, which is then expanded in Extended Data

Fig. 5d to provide a comparison with the HRTEM maps shown in the main text (Fig. 2g). Notably, the QDs appear as dark in HRTEM, demonstrating the validity of the framework used for the analysis discussed in the main text.

Extraction of transport efficiency from PLQE and PL-decay

We define the total transfer efficiency (η_{tot}) and diffusion transport efficiency (η_{diff}) as:

$$\eta_{tot} = \frac{n_{trans}}{n_{all}} (3)$$

$$\eta_{diff} = \frac{n_{diff}}{n_{all}} (4)$$

where n_{trans} stands for the number of charge carriers that are transferred into the quantum dots from the perovskite; n_{diff} is the number of carriers that reach the quantum dots by diffusing across the perovskite matrix; n_{all} is the total amount of photogenerated charge carriers in the perovskite.

Experimentally, η_{tot} can be extracted from photoluminescence quantum efficiency (PLQE) measurement with a modified method reported in literature[17]. We measured the PL from quantum dots in matrix using two excitation wavelength: a short wavelength which can excite both quantum dots and perovskite, and a long wavelength that can only excite quantum dots. The PL of quantum dots in these two scenarios can be written as:

$$PL_{QDs,short} = \left(A_{QDs,short} + \eta_{tot} A_{P,short}\right) \cdot PLQE_{QDs} \cdot I_{ex,short} (5)$$

$$PL_{QDs,long} = \left(A_{QDs,long}\right) \cdot PLQE_{QDs} \cdot I_{ex,long} (6)$$

PL_{QDs} and I_{ex} represent the photoluminescence yield from the quantum dots (in photons/sec) and the photon intensity of the excitation source (also in photons/sec), respectively. A_{QDs} and A_P are

the absorption of quantum dots and perovskite, respectively. A_{QDs} was determined by measuring the change in absorbance at the dot's excitonic peak and scaling the total material absorbance at the chosen wavelength by this factor. A_P was then determined through the additive property of absorbances for a mixture. The Beer-Lambert law was used to convert experimental absorption measurements to absorbances for use in these calculations. In particular, due to very low optical density for the absorption of quantum dots in films with low CQD concentration, the values of A_{QDs} have been estimated by linear scaling (according to the CQD concentration) using the measured one for a film with 28% CQD concentration (highest loading). The PLQE is calculated using an integrating sphere and following a method described elsewhere[18]. The intensity of the excitation source was measured using a power meter (LaserStar). The wavelength-dependent response of the visible and near-infrared photon detectors (for PL and PLQE measurements) were corrected using an Ocean Optics LS-1 calibration lamp with known spectral profile. The short and long in the subscript stands for the corresponding wavelength regime. From Eqs. 5 and 6, we can write:

$$\eta_{tot} = \left[\left(\frac{PL_{QDs,short}}{PL_{QDs,long}} \cdot \frac{I_{ex,long}}{I_{ex,short}}\right) \cdot A_{QDs,long} - A_{QDs,short}\right] \frac{1}{A_{P,short}} \quad (7)$$

The CQD PL scans used to extract the total integrated PL intensity (normalized with the incident light intensity I_{ex}) $\frac{PL_{QDs}}{I_{ex}}$ at different wavelengths are plotted in Figs. S18a and S18b. Due to the presence of a detector cutoff at long wavelength (~ 1380 nm), the integrated area of the left half-peak (shaded area in Figs. S18a and S18b) has been evaluated as $PL_{QDs} = \int_{1000\,nm}^{\lambda_{peak}} PL(\lambda)\, d\lambda$ and then doubled to find the total PL. The absorption scans used to extract the absorption coefficients

A_{QDs} and A_P are also plotted in Extended Data Fig. 7e, and the calculated result are presented in Extended Data Fig. 11b.

Dynamical model for time-resolved photoluminescence

For the perovskite matrix, considering bimolecular recombination as the dominant radiative relaxation pathway,[19] the photoluminescence intensity of perovskite can be written as:

$$\mathrm{I}_{\mathrm{PL}}^{1}(\mathrm{t}) = \mathrm{k}_{\mathrm{rad1}}[n_1(\mathrm{t})]^2 (8)$$

k_{rad1} is the bimolecular recombination rate of perovskite, and $\mathrm{n}_1(\mathrm{t})$ is charge carrier density in perovskite, whose time evolution is modeled as arising from two contributions: a fast exponential decay (carriers rapidly transferred to dots) plus a slower radiative decay:

$$\mathrm{n}_1(\mathrm{t}) = \mathrm{A}_1\mathrm{e}^{-k_{CT}\cdot t} + \frac{1}{k_{rad1}t+A_2} (9)$$

where A_1, $\mathrm{A}_2$are constants; k_{CT} is charge carrier transfer rate, corresponding to the reciprocal of the average time for a carrier to reach (and get captured by) a quantum dot via diffusion in the matrix. From Eq. 8 and 9, the PL intensity of perovskite is:

$$\mathrm{I}_{\mathrm{PL}}^{1}(\mathrm{t}) = \mathrm{k}_{\mathrm{rad1}}[\mathrm{A}_1\mathrm{e}^{-k_{CT}\cdot t} + \frac{1}{k_{rad1}t+A_2}]^2 (10)$$

For quantum dots in matrix, both exciton recombination (triggered by the direct excitation of excitons in dots) and bimolecular recombination (due to free carriers injected from the matrix) contribute to photoluminescence:

$$\mathrm{I}_{\mathrm{PL}}^{2}(t) = k_{ex-rad}n_{ex}(t) + \mathrm{k}_{\mathrm{rad2}}[n_2(\mathrm{t})]^2 (11)$$

$k_{ex-rad}$is exciton radiative recombination rate;k_{rad2} is thebimolecular recombination rate of free carriers in quantum dots; n_{ex} and $n_2(t)$ represent the exciton and charge carrier density, respectively. The exciton density and free carrier density can be written as:

$$n_{ex}(t) = n_{ex0} \cdot e^{-k_{ex} \cdot t} (12)$$

$$n_2(t) = \frac{1}{k_1 t + A_3} (1 - e^{-k_{CT} \cdot t}) (13)$$

n_{ex0} represents the initial exciton density; k_{ex} and $k_1$are total recombination rate of exciton and free charge carrier constants and k_{CT} is the same charge transfer rate as defined in Eq. 9.

Considering equation 11, 12, and 13, the photoluminescence intensity of quantum dots can be written as:

$$I_{PL}^2(t) = k_{ex} \cdot n_{ex0} \cdot e^{-k_{ex} \cdot t} + k_{rad2} [\frac{1}{k_1 t + A_3} (1 - e^{-k_{CT} \cdot t})]^2 (14)$$

These models (Eq.10 and 14) are used to fit the PL decay traces of quantum dots and perovskite and extract the parameters that are most relevant for charge transport, loss, and recombination across the film

Extended Data Fig. 8 shows the integrated photoluminescence from the exciton term in supplementary equation 12 as:

$$\widetilde{PL}_{ex} = \int k_{ex} \cdot n_{ex0} \cdot e^{-k_{ex} \cdot t} dt (15)$$

As well as the integrated PL from free carrier recombination, given by:

$$\widetilde{PL}_{ca} = \int k_{rad2} [\frac{1}{k_{rad2} t + A_3} (1 - e^{-k_{CT} \cdot t})]^2 dt (16)$$

Estimate of carrier diffusion length in perovskite matrix

In general, the diffusion length L_D of carriers in any material can be calculated from the diffusion coefficient D and the carrier lifetime τ using:

$$L_D = \sqrt{D \cdot \tau} \quad (17)$$

Using the experimentally determined carrier lifetime in the perovskite matrix (evaluated from the decay time of the perovskite PL emission, see Fig. 4d in the main text), we can estimate the diffusion length for carriers in our PHC films for different possible values of the diffusion coefficient (which cannot be directly measured) in the range previously determined in pure lead iodide perovskite films[20]. The corresponding data points for L_D, as a function of CQD volume concentration are shown in Extended Data Fig. 10. It can be seen how the estimated values for L_D are comparable to the calculated interdot average spacing (red trace), suggesting that the diffusion length in the matrix is ultimately determined by the average free space available for carriers to diffuse in the matrix before being transferred to the CQDs.

References:

1. Hines, M.A. & Scholes, G. D. Colloidal PbS nanocrystals with size-tunable near-infrared emission: observation of post-synthesis self-narrowing of the particle size distribution. *Adv. Mat.* **15,** 1844–1849 (2003).

2. Perdew, J. P., Burke, K. & Ernzerhof, M. Generalized gradient approximation made simple. *Phys. Rev. Lett.* **77,** 3865-3868 (1996).

3. VandeVondele, J. & Hutter, J.Gaussian basis sets for accurate calculations on molecular systems in gas and condensed phases. *J. Chem. Phys.* **127,** 114105 (2007).

4. Leitsmann, R., Bhm, O., Plnitz, P., Radehaus, C., Schaller, M. & Schreiber, M. *Surf. Sci.*

604, 1808-1812 (2010).

5. Takaluoma, T. T., Laasonen, K. & Laitinen, R. S. Molecular dynamics simulation of the solid-state topochemical polymerization of S_2N_2. *Inorg. Chem.* **52,** 4648-4657 (2013).

6. Bork, N., Loukonen, V. & Vehkamki, H. Reactions and reaction rate of atmospheric SO_2 and $O^-_3(H_2O)_n$ collisions via molecular dynamics simulations. *J. Phys. Chem. A* **117,** 3143-3148 (2013).

7. Smecca, E., Motta, A., Fragal, M. E., Aleeva, Y. & Condorelli, G. G. Spectroscopic and theoretical study of the grafting modes of phosphonic acids on ZnO nanorods. *J. Phys. Chem. C* **117,** 5364-5372 (2013).

8. Hartwigsen, C., Goedecker, S. & Hutter, J. Relativistic separable dual-space Gaussian pseudopotentials from H to Rn. *Phys. Rev. B* **58,** 3641-3662 (1998).

9. Press, W. H., Teukolsky, S. A., Vetterling, W. T. & Flannery, B. P. *Numerical Recipes 3rd Edition: The Art of Scientific Computing.*(Cambridge University Press, NY, USA, 2007).

10. Liu, W., Li, J. C., Zheng, W.T. & Jiang, Q. Ni Al (110)/Cr (110) interface: A density functional theory study. *Phys. Rev. B* **73,** 205421 (2006).

11. Zherebetskyy, D. *et al.* Hydroxylation of the surface of PbS nanocrystals passivated with oleic acid. *Science* **344,** 1380-1384 (2014).

12. Buin, A. *et al.* Materials processing routes to trap-free halide perovskites. *Nano Letters* **14,** 6281-6286 (2014).

13. Haruyama, J., Sodeyama, K., Han, L. & Tateyama, Y. Termination dependence of tetragonal $CH_3NH_3PbI_3$surfaces for perovskite solar cells. *J. Phys. Chem. Lett.* **5,** 2903-2909 (2014).

14. Bian, K., Bassett, W., Wang, Z., & Hanrath, T. The Strongest Particle: Size-Dependent

Elastic Strength and Debye Temperature of PbS Nanocrystals *J. Phys. Chem. Lett.* **5,** 3688–3693 (2014).

15. Feng, J. Mechanical properties of hybrid organic-inorganic $CH_3NH_3BX_3$ (B = Sn, Pb; X = Br, I) perovskites for solar cell absorbers. *APL Mat.* **2**, 081801 (2014).

16. Wise, F. W. Lead salt quantum dots: the limit of strong quantum confinement. *Acc. Chem. Res.* **33**, 773–780 (2000).

17. Tikhomirov, G. *et al.* DNA-based programming of quantum dot valency, self-assembly and luminescence. *Nature Nanotech.* **6**, 485-490 (2011).

18. de Mello, J.C., Wittmann, H.F. & Friend, R.H. An improved experimental determination of external photoluminescence quantum efficiency. *Adv. Mater.* **9,** 230-232 (1997).

19. Manser, J.S. & Kamat, P. V. Band filling with free charge carriers in organometal halide perovskites. *Nature Photon.* **8,** 737-743 (2014).

20. Stranks, S. D.,*et al.,* Electron-Hole Diffusion Lengths Exceeding 1 Micrometer in an Organometal Trihalide Perovskite Absorber. *Science* **342**, 341-344 (2013).

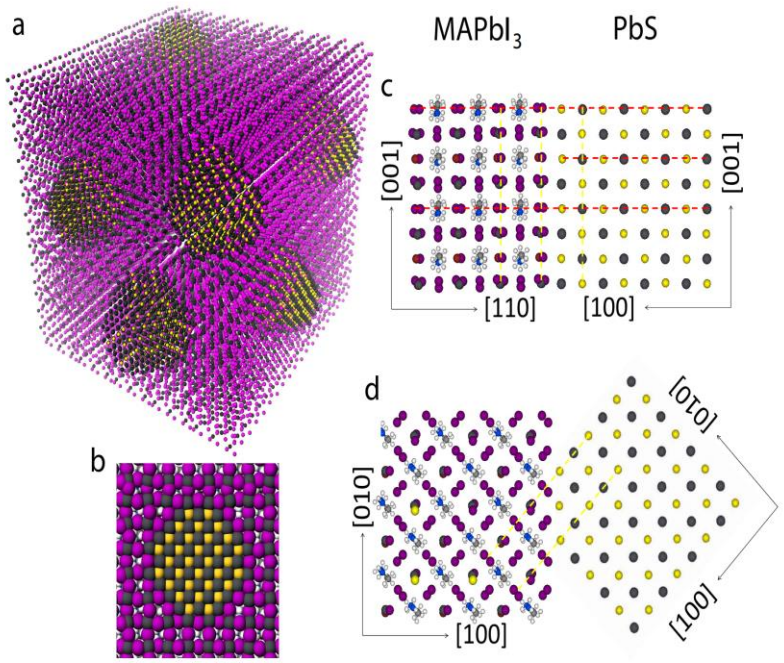

Figure 1| Theoretical model of perovskite epitaxial growth on colloidal quantum dots (CQDs). a, Atomistic model of CQDs in perovskite matrix in three dimensional (3D) view. **b**, Cross-section (2D view) scheme of single CQD in perovskite. All facets of CQDs can match well with perovskite. **c,d**, Modelling of PbS and $MAPbI_3$ crystal structure and their interface, showing that perovskite can match well with PbS from both Z axis [**001**] and X-Y axis [**010**].

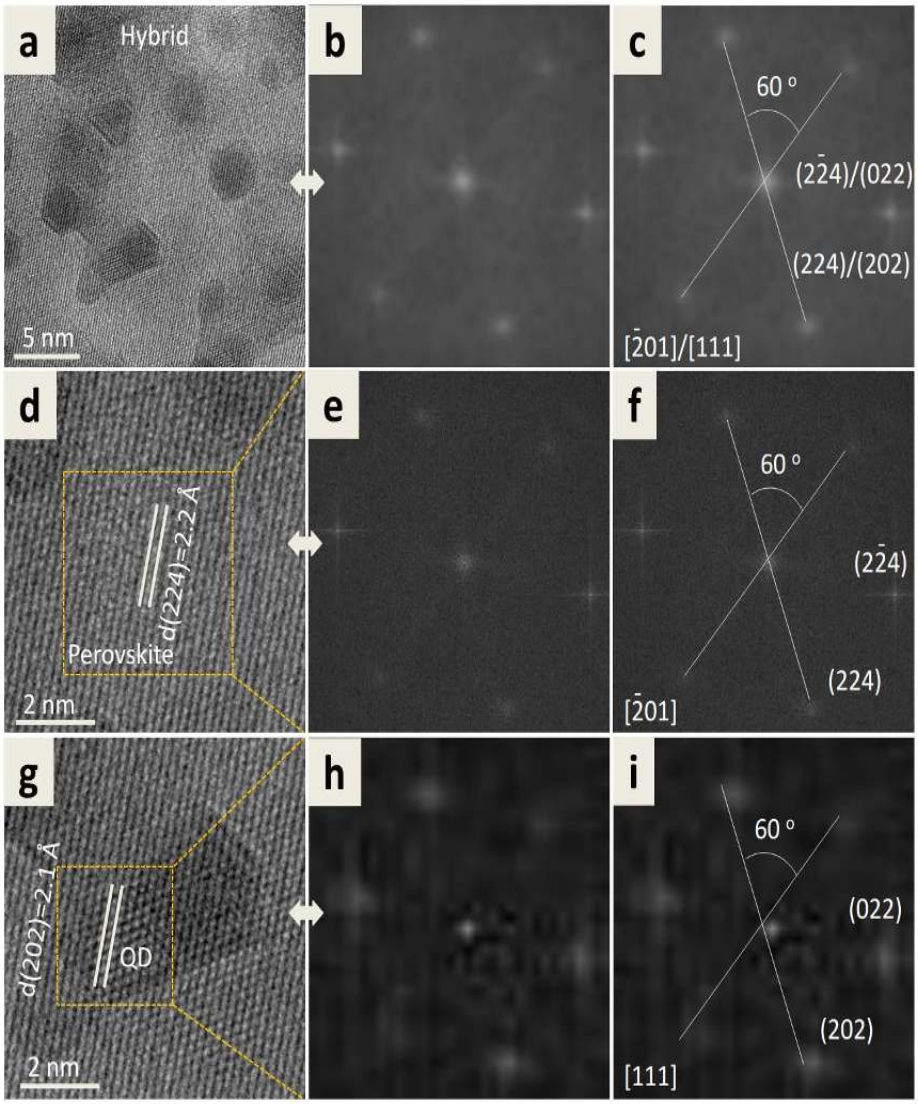

Figure2 | High resolution transmission electron microscopy (HRTEM) images. CQD:Perovskite hybrid (CQDs volume percentage: 3.9%) **(a,b,c)**, $MAPbI_3$ **(d,e,f)**, and CQDs **(g,h,i)** are shown separately. For perovskite, the lattice fringes are indexed to the (224) facets. For CQD, the lattice fringe is indexed as (022) facet. In real space, the d-spacing value of the (224) facet of perovskite (2.2 Å) matches well with the (111) facet of PbS (2.1 Å). This is consistent with the modeling, which shows that the (100) facet of PbS matches well with (110) facet of perovskite. The FFT image shows the same intersection angle (60 degree) for both perovskite and CQDs, indicating that they can match not only two dimensionally, but also three dimensionally, confirming again that perovskite and CQDs have the same orientation.

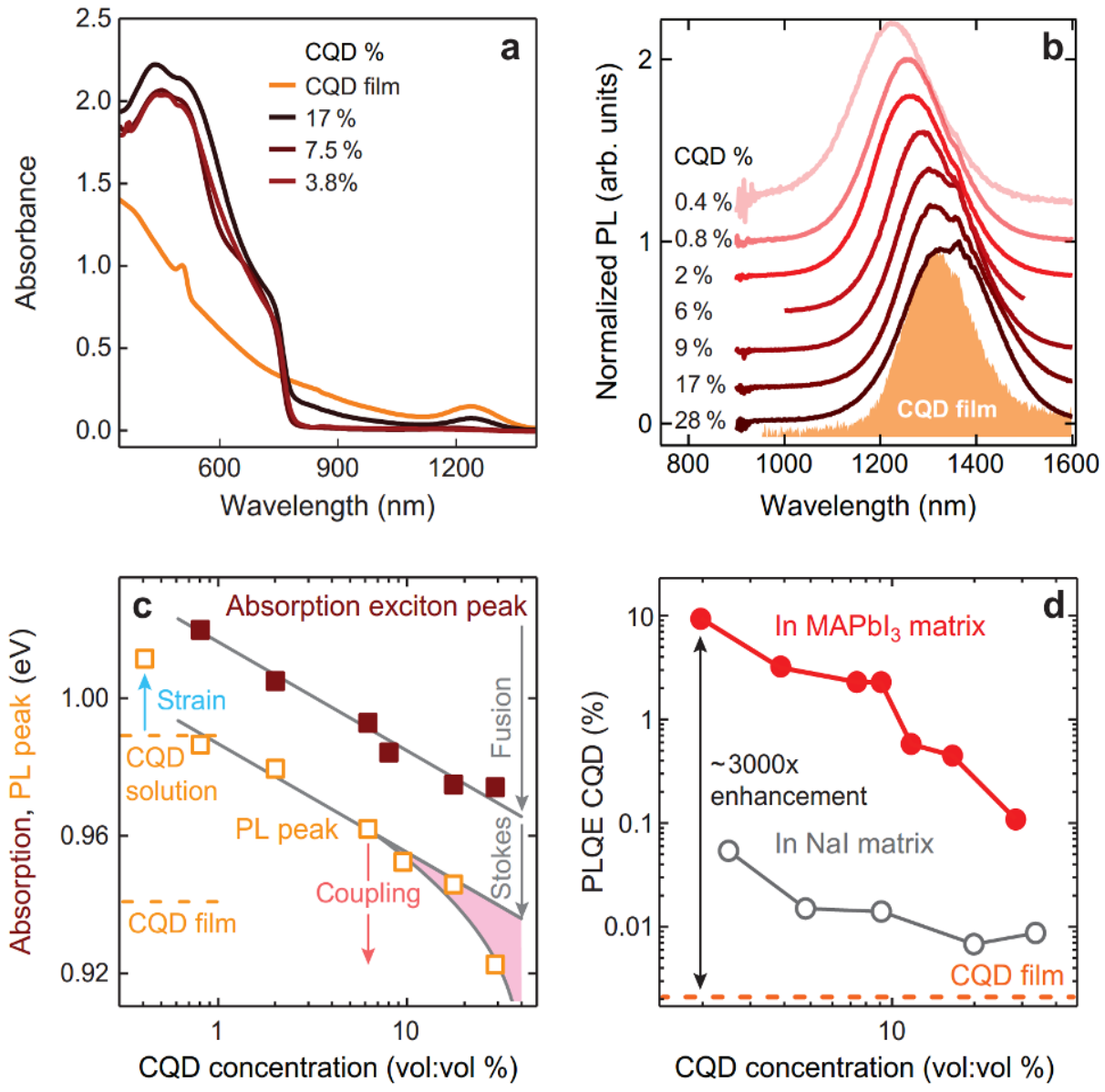

Figure 3| Photophysical response of CQD:perovskite hybrid. a,b, Matrix-tuned absorption **(a)** and photoluminescence **(b)** of CQD:perovskite hybrid. After the growth of perovskite, a representative absorption edge around 770 nm appears, while both absorption and photoluminescence (PL) CQD exciton peaks are preserved, indicating that the properties of CQDs remain unaltered. **c,** CQDs absorption and PL exciton peak position shift as a function of CQD:$MAPbI_3$ ratio, with different concentration-dependent mechanisms highlighted. **d**, PL quantum efficiency (PLQE) of CQDs in matrix. For lower CQD concentration the PLQE is

increased, indicating that CQDs are well dispersed in the matrix and carrier dissociation between CQDs is blocked. In the $MAPbI_3$ matrix, the PLQE is two orders of magnitude higher than that in a NaI matrix, which reveals that a lattice-mismatched matrix (8.8% mismatch for NaI) cannot grow on PbS. This finding confirms that epitaxial growth of matrix on CQDs is critical for CQD surface passivation. The PLQE of a solution-exchanged CQD film (orange dashed line) is shown for comparison.

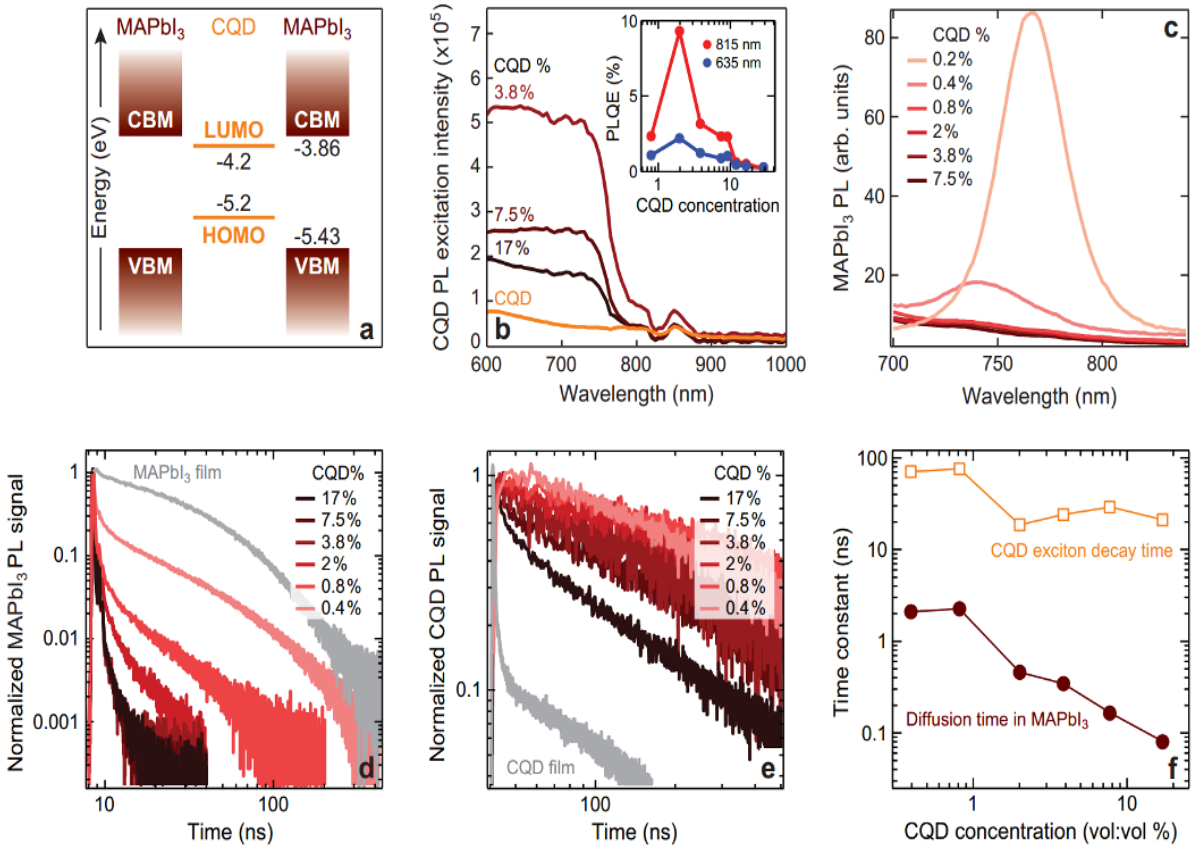

Figure 4 | Carriers transfer from perovskite to CQDs. a, Electronic band structure of CQDs and perovskite. The LUMO level of CQD is lower than the conduction band of perovskite and the HOMO level position of CQD is higher than the valence band of perovskite, making the transfer of both carriers from perovskite to CQDs energetically favored. **b**, CQDs PL excitation spectra. In the perovskite absorption region ($\lambda < 780\,nm$), for increasing perovskite content the PL excitation intensity is enhanced, indicating that carriers excited in perovskite are transferred to

CQDs. However, considering the partial carrier loss (via recombination) in perovskite, the PLQE of the hybrid is lower than the internal PLQE of CQD when long excitation wavelength is used (inset). **c**, PL spectra of $MAPbI_3$ for PHC films with different CQDs concentration. **d,e,f,** Transient PL emission from $MAPbI_3$ (d) and CQDs (e) and corresponding time constants (f). As the CQD:$MAPbI_3$ is reduced, the initial PL decay time of both perovskite and CQDs become longer, as a result of longer transit time in the matrix and reduced carriers dissociation across the CQDs, respectively.

Extended Data Figure 1 | Planar averaged total charge difference with respect to the pristine slabs.

Extended Data Figure 2 | DFT simulation. a, Highest Occupied Molecular Orbital (HOMO); **b,** the Lowest Unoccupied Molecular Orbital (LUMO) (right) of matched quantum dot; and **c,** (HOMO), **d,** (LUMO) of mismatched dots. The states are mostly localized in CQD in matched dots, while are localized on the interface between CQD and perovskite, indicating the formation of defects in the mismatched quantum dots. **e,** The density of state (DOS) of CQDs that match with perovskite, and the states are mostly localized in CQD; **f,** DOS of mismatched CQDs, states of which are localized on the interface between CQD and perovskite, indicating the formation of defects.

Extended Data Figure 3 | DFT simulation of strain distribution in PHC composite material. **a,** Cross-section of the relaxed 3 nm PbS CQD in vacuum; **b,** DFT-optimized geometry of the same 3 nm CQD epitaxially matched with perovskite in a unit cell corresponding to unstrained perovskite.

Extended Data Figure 4 | Compositional analysis of PHC. a, b, c, d XPS analysis of the CQDs embedded PHC film. All corresponding elements are observed in the film, indicating the existence of both PbS and $MAPbI_3$; **e,** XPS spectra of the N1s region for high loading PbS films, following the ligand exchange to perovskite ligands in butylamine, before the methylammonium post-treatment step. We detect only the ammonium signal at 402 eV and no amine signal at 398-399

eV, suggesting that methylammonium iodide ligand is more stable on surface and displaces weakly-bound buylamine, even before film annealing. **f,** Plot of the nominal volume ratio of CQDs to perovskite versus the ratio measured using Rutherford backscattering spectroscopy (RBS), with linear fit (red line) superimposed. The ideal case of the measured ratio equalling the nominal ratio is shown by the dashed grey line, showing the excellent agreement between the nominal value and the one evaluated from by RBS.

Extended Data Figure 5 | TEM images of PHC. HAADF-STEM images of **a,** pure perovskite and **c,** dots in perovskite; **b,** TEM images of pure perovskite and dots in perovskite (inset of **c** and zoomed-in view in **d**). The circle in **c** marks an area in which three PbS nanocrystals (white spots) located inside perovskite crystal (grey area).

Extended Data Figure 6 | Microscopic images. a, TEM image of CQDs after solution phase iodide ligands exchange. The average CQD size is ~4 nm. **b,** Scanning electron microscopy (SEM) image of the film surface with CQDs embedded in perovskite matrix (CQD volume percentage of 3.8%). The average perovskite grain size is about60 nm. **c,** Cross section SEM image of the film with CQDs embedded in perovskite matrix (CQD volume percentage of 3.8%). The film thickness is about 240 nm (top layer). **d, e,** Simulated TEM image of matched (**d**) and mismatched (**e**) CQDs and perovskite.

Extended Data Figure 7 | Absorption and photoluminescence properties of PHC. a, b, absorption and photoluminescence spectra for a pure CQD film (**a**) and a pure perovskite film (**b**). **c, d, e,** CQD photoluminescence signal from PHC films with 28% (**c**) and 17% (**d**) CQD concentration, acquired at $\lambda = 635$ nm (blue), 680 nm (green), and 815 nm (red). The PL signal has been normalized by the excitation intensity at the different wavelengths used. The shaded area marks the region of the spectrum considered for the calculation of the PL integrated area used in Eq. 7. (**3**) Corresponding optical absorption spectra for a CQD concentration of 28% (dark red) and 17% (red) which were used for the evaluation of the absorption parameters used in Eq. 7.

Extended Data Figure 8 | Integrated CQDs photoluminescence contributions. Filled markers represent the integrated PL contribution due to free carriers injected from the perovskite, while hollow markers represent the integrated PL due to the dissociation of excitons generated directly in the CQDs (see also Eq. 10). Both free carrier and exciton recombination increase with decreasing CQD concentration. Consistent with the PL excitation spectra, the largest contribution to the CQDs PL can be ascribed to radiative recombination of free carriers transferred from the perovskite.

Extended Data Figure 9 | Photophysical dynamics of PHC. a, PL excitation profile from a hybrid film of 1300 nm CQDs dispersed in 950 nm CQDs (1:10 volume ratio), acquired by measuring the PL emission (at $\lambda \sim 1300$ nm) from the small bandgap CQDs as a function of excitation wavelength. The absorption profile from the large bandgap CQDs is overlaid as shaded grey area, exhibiting the characteristic excitonic peak at $\lambda \sim 950$ nm. The wavelength dependence of the PL intensity from the small bandgap CQDs closely follows the absorption profile of the large bandgap CQDs, in analogy with the situation for dots-in-perovskite films (see Fig. 4b in the main text), and is therefore suggestive of carrier funnelling from the large to the small bandgap dots. **b**, PL decay for 1300 nm CQDs in a CQD-based matrix (light red) and in a perovskite ($MAPbI_3$) matrix (dark red), with 632 nm excitation. The longer dynamics for the quantum dots embedded in the perovskite matrix (~150 ns) vs. dots-in-dots (~30 ns) provides evidence for a better passivation of CQDs in the latter.

Extended Data Figure 10 | CQD concentration dependent diffusion length. Plot of the diffusion length L_D of carriers in the perovskite matrix (round markers) for various CQD concentrations, calculated using Eq. 17 and different possible values for the diffusion coefficient (see legend). The red trace also shows the calculated average interdot spacing as a function of CQD:$MAPbI_3$ volume ratio.

Extended Data Figure 11 | Composition and photophysical parameters of quantum-dot-in-perovskite solid. a, List of the values for the nominal $MAPbI_3$ to PbS mass ratio (first column) and volume ratio (second column), PbS to $MAPbI_3$ volume ratio (third column), and PbS volume percentage over total volume (fourth column). The experimental values for the PbS volume percentage over total volume, as extrapolated from a fit to the RBS data (see also Fig. S9) are shown in the fifth column. **b,** Numerical values of the photophysical parameters entering Eqs. 5-7 and leading to the evaluation of the carrier transfer efficiency.